

## Deep learning solutions for domain-specific image segmentation

Vadineanu, S.

### Citation

Vadineanu, S. (2025, October 8). *Deep learning solutions for domain-specific image segmentation*. Retrieved from https://hdl.handle.net/1887/4266937

Version: Publisher's Version

License: License agreement concerning inclusion of doctoral thesis

in the Institutional Repository of the University of Leiden

Downloaded from: <a href="https://hdl.handle.net/1887/4266937">https://hdl.handle.net/1887/4266937</a>

**Note:** To cite this publication please use the final published version (if applicable).

## Chapter 2

# Annotation Errors in Cell Segmentation

## 2.1 Introduction

Image segmentation, i.e., the labelling of relevant features in images, has been an important topic for the computer vision community [62]. In recent years, the use of deep convolutional neural networks for image segmentation has become increasingly popular [3]. Although such algorithms are able to achieve similar performance to human annotators on certain tasks [51], they are heavily dependent on both the quantity and the quality of the training data. The importance of quality is especially prominent in the context of segmentation, where the annotation process is time-consuming and often requires domain-expert knowledge (e.g., in medical imaging). One important issue that arises is the high variability between expert annotators when segmenting anatomical structures from medical images [13, 94, 175]. For instance, the segmentation of multiple sclerosis poses difficulties to many experts since the lesion area can vary in size, shape or location [174], inducing high inter- and intra-observer variabil-

This chapter is based on:

S. Vădineanu, D. M. Pelt, O. Dzyubachyk, and K.J. Batenburg. "An analysis of the impact of annotation errors on the accuracy of deep learning for cell segmentation". *International Conference on Medical Imaging with Deep Learning (pp. 1251-1267)*. PMLR (2022).

#### 2.1. Introduction

ity [22]. Also, there can be a considerable amount of disagreement between experts when defining the segmentation border of the optic nerve head in retinal images [49]. These annotation dissimilarities can mean that the manually annotated labels used for segmentation may deviate from the ground truth, which can negatively impact the accuracy of the supervised machine learning models.

In order to compensate for such inconsistencies, various label fusion techniques, e.g., STAPLE [165], VoteNet [47], have been proposed to extract an approximation of the ground truth from multi-expert annotations. However, such methods often require multiple opinions for the same data, a process that is costly and slow. In addition to the effort that the research community is putting into alleviating the label inconsistency issue, it is also important to study the actual impact that such label imperfections are causing to the segmentation algorithms. The benefits of such a study are twofold. Firstly, the engineers who use existing deep learning solutions when developing tools would learn whether they can reduce the expert time on annotations by admitting lower quality labels and still achieving the desired results. Secondly, the developers of deep learning techniques can be provided with insights indicating ways to design more robust algorithms with respect to annotation errors.

While the literature proposes multiple methods to mitigate the effect of annotation errors in image segmentation, there are few works evaluating the concrete implications of these errors. In particular, [179] develop a measurement of label quality in the context of semantic segmentation of synthetic urban street view scenes. They apply various levels of simplifications to the segmentation masks of the scene and use a modified version of FusionNet [120] and FCN16 [131] to generate the predictions. Their results emphasized the need for a large set of coarsely annotated images rather than strongly controlling the label quality. However, the study assumes the immediate availability of a large pool of unannotated images with an inexpensive coarse annotation process, which is often impossible to achieve in medical imaging, where even creating coarse labels requires a certain extent of expertise. [67] emulated three types of perturbations on a liver segmentation data set [17]. The errors included the application of random offsets, shifts and flips of pixel labels applied to the annotation images, while the evaluation was performed for UNet [125], SegNet [11] and FCN32 [131]. The selection of errors was further diversified by [156] with their work on an MRI brain tumour data set [68]. They made use of elastic transformations, random crops of the tumour area, constant shifts and random permutations between slices and their labels. Consequently, they observed the effects of the perturbations for multiple learning paradigms based on a UNet backbone. Both studies introduce errors present-

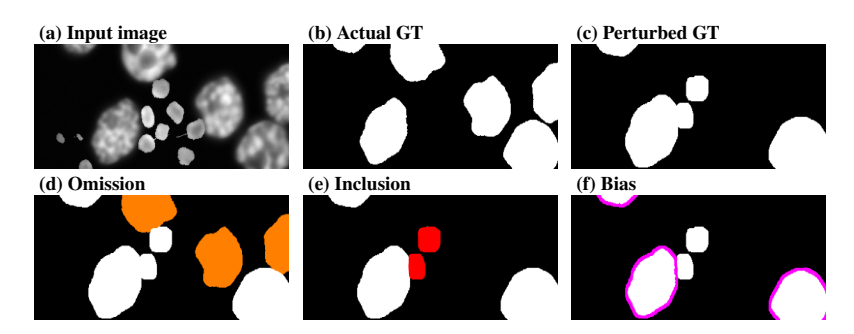


**Figure 2.1:** Example of our proposed perturbations. Figure (a) shows an input image where the HL60 cells are the target objects and the granulocytes form the background objects. The unmodified ground truth is shown in (b), and its perturbed version in (c). The errors are highlighted in (d) – omission/orange, (e) – inclusion/red and (f) – bias/purple.

ing plausible occurrence scenarios. However, each of them is performed on a single manually-annotated data set, whose labels can already be subjected to the errors the authors try to model.

In this chapter, we extend previous works by introducing three error-emulation techniques applied to three different data sets. So far, the current annotation error studies on biomedical images have been focusing on segmentation tasks of unitary objects (e.g., organs, tumours). Such objects are limiting most error emulation approaches to create perturbations only at the border of the object's label. We deviate from this approach by proposing an analysis of sparsely distributed objects in the context of cell segmentation. This enables us to not only induce errors at the border of the objects, but also to emulate errors concerning entire regions, such as the complete removal or addition of cells. In addition, we address the shortcomings of using manual annotations as ground truth by employing two perfectly-annotated synthetic data sets of HL60 and granulocytes [140] and validate our observations on manually-annotated microscopy images [153]. Moreover, we expand the current analysis by incorporating a network whose architecture diverges from the usual encoder-decoder paradigm.

## 2.2 Background and Methodology

Our analysis is focused on the segmentation task of 2-dimensional vector-valued (e.g., RGB) images, denoted as arrays of pixels  $x \in \mathbb{R}^{N \times M \times C}$ , where N, M, C represent the number of rows, columns and channels, respectively. The aim is to find a mapping from x to an output  $y \in \mathbb{Z}^{N \times M}$  that subdivides the image into disjoint sets of pixels,

### 2.2. Background and Methodology

each set corresponding to a certain category. In our work, we address the problem of binary cell segmentation by separating only one class of objects from the background. Suppose the image x contains E cells. For each cell i we define the cell label  $l^i$  as the binary image in which the pixels belonging to that cell are set to one and all other pixels set to zero:

$$l_{nm}^{i} = \begin{cases} 1, & \text{if } x_{nm} \text{ belongs to cell } i \\ 0, & \text{otherwise} \end{cases} \quad \forall \ 1 \le n \le N, \ 1 \le m \le M.$$
 (2.1)

Given the set of all cell labels  $\mathcal{L} = \{l^1, l^2, \dots, l^E\}$ , a target image for training can be constructed by:

$$y = \sum_{l \in \mathcal{L}} l \tag{2.2}$$

In order to approximate the desired mapping, we employ convolutional neural networks (CNNs) by passing the input image through a series of successive operations, called layers. The networks are given a set of input images  $X = \{x_1, x_2, \dots, x_{N_t}\}$  and the predicted output  $\hat{Y} = \{\hat{y}_1, \hat{y}_2, \dots, \hat{y}_{N_t}\}$  is compared against the target output  $Y = \{y_1, y_2, \dots, y_{N_t}\}$  with the goal of minimizing a loss function.

Annotation errors. As the true output usually comes from manual annotation, it becomes subjected to human errors, which can hinder the training of CNNs. We model such inconsistencies and separate them into three categories (shown in Figure 2.1) as follows:

Omission Errors. Typical stained tissue scans can include tens or even hundreds of cells of different shapes and sizes [46]. When creating segmentation masks for such diverse and populated images, it is possible that an expert annotator may unintentionally ignore a certain proportion of the relevant cells. We call such absence of cell annotations omission errors and we develop a systematic method of altering the ground truth mask by removing a ratio of the present cells from the label set  $\mathcal{L}$ . An example of cell removal is showcased in Figure 2.1(d). We define  $\mathcal{L}^{S} \subseteq \mathcal{L}$  as a random subset of size  $S \subseteq \mathcal{E}$ , where S is chosen to satisfy the omission rate  $r_{\omega} = \frac{S}{E}$ . The label after omission is comprised of the binary labels corresponding to the remaining cells  $y^{\omega} = \sum_{l \in \mathcal{L} \setminus \mathcal{L}^{S}} l$ .

Inclusion Errors. Another issue that can arise in tissue scans is the accidental annotation of cells belonging to the wrong category. In such cases, an annotator might sometimes include some fundamentally different cells due to their proximity or apparent resemblance to the correct cells. We incorporate this inclusion error into

our analysis with various amounts of severity, which correspond to the amount of "wrong" cells that we choose to include in the label set. One such case is presented in Figure 2.1(e). We define  $\Lambda = \{\lambda^1, \lambda^2, \dots, \lambda^F\}$  as a set of binary labels for other objects within x and  $\Lambda^S \subseteq \Lambda$  as a random subset of size  $S \subseteq F$ , where S is chosen to satisfy the inclusion rate  $r_\phi = \frac{S}{F}$ . The resulting subset is then added to the label set  $\mathcal{L}$  before creating the final label  $y^\phi = \sum_{l \in \mathcal{L} \cup \Lambda^S} l$ .

Bias Errors. Another important factor that deserves attention is the ambiguity that is often present when delimiting the cell borders. Often, it is difficult for annotators to precisely distinguish the true outline of cells. This can lead to annotations that deviate from the gold standard (ground truth), inducing bias into the data. Such biases can manifest in the form of creating cell labels that excessively cover the actual cell surface, as can be observed in Figure 2.1(f). Moreover, the opposite can also happen, when the annotator "shrinks" the corresponding label relative to the true area of the cell. We consider both cases in our study and we also control the amount of bias we introduce by expanding and reducing the sizes of the cell labels that are present in our data sets. In order to model the annotation bias, we employ morphological operations [130]. Specifically, we simulate excessively covering cells by applying a dilation operation  $\oplus$  to the target image y a number of q times, where q is randomly chosen between 1 and  $q_{\text{max}}$ . Similarly, we simulate the shrinking of cells by applying an erosion operation  $\ominus$  q times, where q is randomly chosen between 1 and  $q_{\text{max}}$ .

## 2.3 Experiments

## 2.3.1 Experimental Setup

In this work, we considered three types of convolutional neural networks based on their wide adoption and distinctive characteristics. Our selected networks include:

- **UNet** [125] encoder/decoder architecture, decoder with transposed convolutions, direct connections between the encoder and decoder;
- **SegNet** [11] encoder/decoder architecture, decoder with unpooling, no connections between the encoder and decoder;
- Mixed-scale dense network (MSD [116]) densely connected architecture, dilated convolutions.

We performed our experiments using PyTorch [114] implementations of our chosen network architectures, while keeping their structure, e.g., the number of layers, similar

### 2.3. Experiments

to their original implementation. For our two-class segmentation problem, the true output will be a two-channel image, where a pixel on the first channel is 1 if it corresponds to a pixel of the background and 0 otherwise, while the reverse is true for the second channel. A soft-max activation is used on the output of the final layer, while all intermediate layers are paired with a ReLU function. We aim to minimize the Dice loss by using ADAM optimizer [82] while training the network for 20 epochs on the synthetically-generated data and for 50 on the manually-annotated images, the latter epoch count being larger due to the increased complexity of the images. After each epoch, the model is tested on a validation set selected as a separate portion of 30% from the training data and the model with the lowest validation score is kept. Our qualitative metric is the Sørensen-Dice coefficient, which we compute for the entire test set and average over 10 runs. Moreover, whenever a network reaches an untrainable state, i.e., it only segments the background, we discard the model and restart training with a different initialization. The performance comparisons were validated using Wilcoxon tests [124].

## 2.3.2 Synthetic Data

These experiments were conducted on simulated microscopy images of HL60 nuclei cells and granulocytes [140]. The images obtained from the Masaryk University Cell Image Collection<sup>1</sup> were generated by a virtual microscope [166]. An image-label sample pair for each data set is shown in Figure 2.2. The different sizes and position distributions of the two cell types make them good candidates for our analysis since the same generated perturbation can affect them differently. This will enable us to apply our observations to a broader variety of cells. For each category of cells, the data set consists of 30 volumes, each volume being separated into 129 slices of 565×807 16-bit pixels. We used 25 volumes for training, while 5 were kept for testing. We selected the slices that had a non-empty label, resulting in an average number of 84 slices per volume. For these data sets, we assume having one annotator per volume, thus, we emulate the errors once per volume.

Omission errors. We perform the omission for  $r_{\omega} \in \{10\%, 20\%, 30\%, 50\%, 70\%\}$ . The results presented in Figures 2.2(e,h) show that this category of errors has limited impact on the networks' performance when we consider moderate cases ( $r_{\omega} \leq 30\%$ ). MSD and UNet show similar robust behaviour to moderate omissions, while SegNet presents a pronounced downward trend, with a 10% reduction in Dice score for 30%

<sup>1</sup>https://cbia.fi.muni.cz/datasets

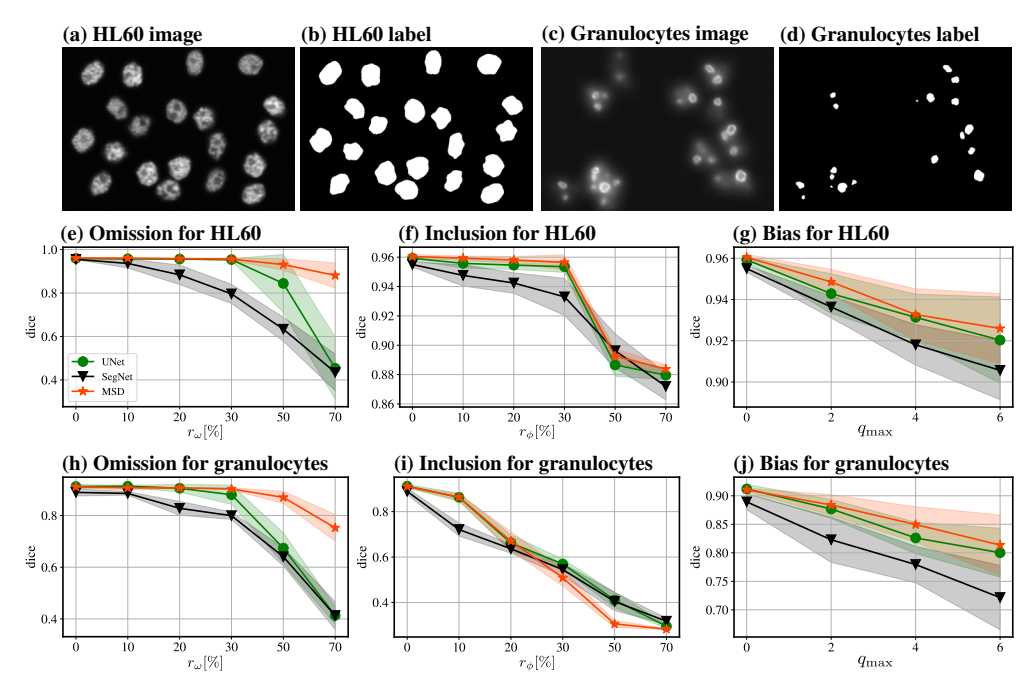


**Figure 2.2:** Example images and results for the synthetic data sets. Figures  $(\mathbf{a}, \mathbf{b})$  and  $(\mathbf{c}, \mathbf{d})$  show image/label pairs of simulated microscopy slices.  $(\mathbf{e}-\mathbf{j})$  show the Dice score of trained networks on the test set as a function of perturbation severity, for HL60 cells  $(\mathbf{e}-\mathbf{g})$  and granulocytes  $(\mathbf{h}-\mathbf{j})$ . Results are shown for: omission  $(\mathbf{e}, \mathbf{h})$ , inclusion  $(\mathbf{f}, \mathbf{i})$ , and bias errors  $(\mathbf{g}, \mathbf{j})$ . The shade around the curves corresponds to the standard deviation of the results.

omission, relative to no omission. For relatively large omissions ( $r_{\omega} > 30\%$ ), MSD maintains a relatively low reduction in performance even for  $r_{\omega} = 70\%$ . However, this comes with the caveat that, for omissions above 30%, the training process of MSD occasionally collapses to an untrainable state. Both the training instability and the limited reduction in accuracy for large omission rates of MSD are a consequence of its design. The low number of parameters required by MSD might enable it to be less prone to overfitting on the wrongly labelled data, but also to become less stable when the label quality is substantially deteriorated.

Inclusion errors. In order to add inclusion perturbations, we merge the volumes of the HL60 nuclei cells and the granulocytes, while defining one data set to be the main one, with its labels being  $\mathcal{L}$ , while the other one becomes secondary, with its labels being  $\Lambda$ . In our experiments, we have  $r_{\phi} \in \{10\%, 20\%, 30\%, 50\%, 70\%\}$ . Figures 2.2(f, i) illustrate that the inclusion perturbation results in different behaviours for the models, depending on the data set it is applied to. In the case of HL60, SegNet

### 2.3. Experiments

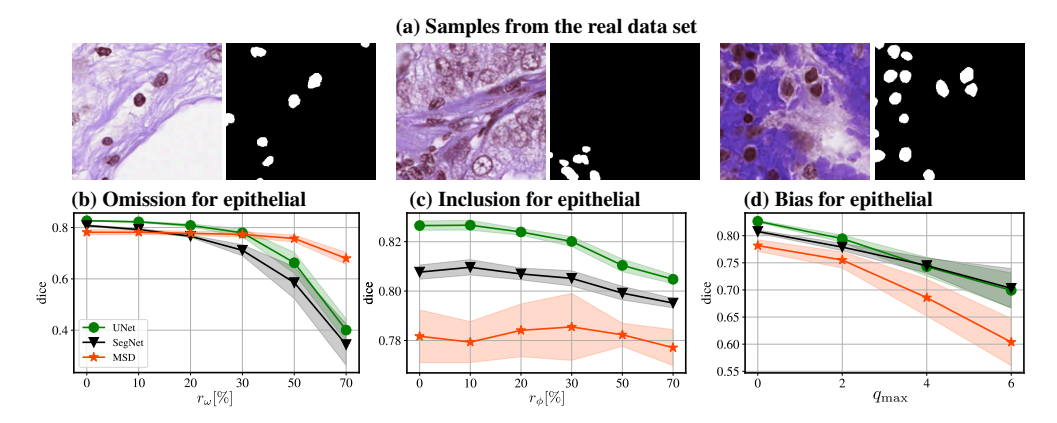


**Figure 2.3:** Example images and results for the manually-annotated data set. Figure (**a**) shows image/label pairs of stained-tissue images. Figures ( $\mathbf{b}$ - $\mathbf{d}$ ) show the Dice score of trained networks on the test set as a function of perturbation severity. Results are shown for: omission (**b**), inclusion (**c**), and bias errors (**d**). The shade around the curves corresponds to the standard deviation of the results.

presents a slow decreasing trend until  $r_{\phi}=30\%$ , while UNet and MSD appear to be unaffected by the moderate inclusion. Also, since the granulocytes occupy a much smaller area in each slice than the HL60 cells, their addition into the latter's volume does not heavily impact the models even for 70% inclusion, resulting in a loss in performance of less than 1%. Moreover, Figure 2.2(i) shows that wrongly including large objects into the segmentation mask severely impacts all networks' capabilities, with an average Dice score drop of 23% for every 10% increase in  $r_{\phi}$ .

Bias errors. For this type of perturbation, we performed our analysis by choosing  $q_{\text{max}}$  from  $\{2, 4, 6\}$ . Figures 2.2(g,j) show that introducing label bias through random morphological operations creates a descending trend for all network architectures. However, this trend presents different magnitudes depending on the data set. In the case of HL60 cells, we observe a decrease in Dice score of up to 5%, while for granulocytes the performance drops to 19%. This decline is a consequence of the much smaller footprint of the granulocytes' labels in relation to the background. Thus, mistakes in the outline of smaller cells are more costly than for their larger counterpart. In addition, we notice here that MSD and UNet perform similarly on the synthetic images, with SegNet lagging behind, by 6% and 10% on average for HL60 (Figure 2.2(g)) and granulocytes (Figure 2.2(j)), respectively.

## 2.3.3 Manually-Annotated Data

Following the observations drawn from the synthetic data we aim to extend them to a segmentation task of manually-annotated stained tissue images. We selected the data set belonging to MoNuSAC 2020 challenge [153], which contains H&E stained tissue images belonging to multiple organs. The data were gathered with the purpose of performing automatic cell segmentation, which can provide crucial information about the organ's health. This data set is comprised of 310 8-bit images of various sizes containing four types of cells: epithelial, lymphocytes, macrophages and neutrophils. Among these types, we selected the epithelial cells to be the target of our task, while considering the rest as background. The selection was motivated by the larger presence of the epithelial cells on a both per-image and per-data-set basis. Hence, we are left with 96 images for training and 37 for testing. Moreover, due to the varying size of the images, an extra preprocessing step was performed. The step involved separating each image into 256×256 patches using a sliding window technique while allowing for an overlap of 64 pixels between patches. A few samples of the selected patches are shown in Figure 2.3(a). Also, given the variability in size, quality and provenience of the data, we assume an individual annotator for every single image. Thus, we will apply our perturbation framework to each image separately.

The omission and bias-inducing processes are performed similarly to the synthetic data. For inclusion, we choose the main type of cells to be epithelial, while the lymphocytes form the secondary category. We chose lymphocytes since their pairing with epithelial cells is the most prevalent in the data set. We show the experimental results in Figures 2.3(b-d). In the case of omission, one notable difference from the synthetic data is the slight performance gap between MSD and the UNet/SegNet pair for  $r_{\omega} < 30\%$ . Nonetheless, this gap decreases the more error we allow, showing MSD to plateau at 77% Dice score until we remove 50% of the cell labels, while the other networks are severely affected (18% and 26% reduction for UNet and SegNet, respectively). When it comes to inclusion, the segmentation performance, similarly to the HL60 cells, appears to be rather unaffected by wrongly labelled additional cells until 30% inclusion. Moreover, the larger rates ( $\geq 50\%$ ) inflict a more modest loss in the Dice score compared to the HL60 volumes due to the poorer fit the models have on real data. Since their learned parameters may not be a perfect fit for the data, the models can allow small perturbations of their input without suffering large losses. The bias on epithelial cells shows UNet and SegNet to develop an increasing gap from MSD, which reaches a 22% reduction in Dice score for  $q_{\text{max}} = 6$ . Here, MSD appears to suffer

#### 2.4. Conclusion

from the lack of complexity since this data set presents a more complex background with high variability between images, impeding, thus, a very good distinction of the correct cells. This tendency is further exacerbated by the perturbations applied to the cells' masks.

## 2.4 Conclusion

Understanding the consequences of labelling errors is of great importance for the field of biomedical image segmentation. Our study provided insights into meaningful issues that can be present in the annotation process for cell segmentation. We emulated three different labelling errors (omission, inclusion and bias) for two perfectly-labelled synthetic data sets and one manually-annotated data set and observed their impact on the results of three networks. We found that wrongly including large objects into the segmentation labels drastically decreases the quality of the predictions, while smaller objects are filtered out more easily when moderately included  $(r_{\phi} \leq 30\%)$ . We also observed that, even in low amount, the presence of bias deteriorates the predictions for all cell types, especially for relatively smaller cells such as granulocytes and epithelial cells. Finally, we observed that moderate omissions ( $r_{\omega} \leq 30\%$ ) present a negligible impact to both MSD an UNet, with the latter slightly outperforming the former on the manually-annotated data set. However, for larger omissions, MSD still retains a competitive Dice score. This robustness to omissions can be exploited in settings where the expert annotator would be required to label just a portion of the present cells, significantly reducing the annotation costs. Also, MSD could be used to preprocess training labels for more complex, but noise-sensitive, learning algorithms.